Symmetry-resolved entanglement of two-dimensional symmetry-protected topological states

Daniel Azses [ORCID],[1] David F. Mross [ORCID],[2] and Eran Sela[1]

[1]*School of Physics and Astronomy, Tel Aviv University, Tel Aviv 6997801, Israel*
[2]*Department of Condensed Matter Physics, Weizmann Institute of Science, Rehovot 7610001, Israel*

Symmetry-resolved entanglement is a useful tool for characterizing symmetry-protected topological states. In two dimensions, their entanglement spectra are described by conformal field theories but the symmetry resolution is largely unexplored. However, addressing this problem numerically requires system sizes beyond the reach of exact diagonalization. Here, we develop tensor-network methods that can access much larger systems and determine universal and nonuniversal features in their entanglement. Specifically, we construct one-dimensional matrix product operators that encapsulate all the entanglement data of two-dimensional symmetry-protected topological states. We first demonstrate our approach for the Levin-Gu model. Next, we use the cohomology formalism to deform the phase away from the fine-tuned point and track the evolution of its entanglement features and their symmetry resolution. The entanglement spectra are always described by the same conformal field theory. However, the levels undergo a spectral flow in accordance with an insertion of a many-body Aharonov-Bohm flux.

I. INTRODUCTION

Symmetry-protected topological states (SPTs) are characterized by a symmetric bulk state that does not host fractional excitations. Still, they are topological in the sense of carrying anomalous edge states at their boundary with a trivial state or different SPTs. In two dimensions, the edges are described by a one-dimensional conformal field theory (CFT) [1–5]. The presence of these states is dictated by a specific structure in their entanglement. Yet, unlike topologically ordered (fractional) states, the entanglement entropy of SPTs does not contain a topological term. Instead, the topological nature of these states may be revealed by resolving the entanglement entropy according to symmetries or by studying entanglement spectra (ES).

The entanglement entropy of a system with global symmetries can be decomposed according to the associated quantum numbers [6–9]. Specifically, it is given by the sum of entropies for each choice of these quantum numbers *in one subsystem*. The Rényi moments of the symmetry-resolved entanglement are experimentally measurable [10–13] as also demonstrated for one-dimensional SPT states [14,15] on IBM quantum computers. For such states, each symmetry sector contributes equally to the total entropy [16]. This equipartition corresponds to exact degeneracies in the ES [17,18]. These have been recognized as the source of the computational power of one-dimensional SPTs [19] within measurement-based quantum computation [20].

The ES generalizes the entanglement entropy and contains additional universal information. For two-dimensional (2D) topological states with a chiral edge, the Li-Haldane conjecture [21,22] states that the levels of the ES correspond to the conformal field theory that describes a physical edge. Extrapolating to the nonchiral case, one may expect that the ES of SPT phases have the same universal properties as their nonchiral

edge CFTs, such as the central charge c. For example, for SPTs stabilized by a $\mathbb{Z}_N$ symmetry, the free-boson CFT with $c = 1$ was found to describe the edge [1,2]. While the ES should correspond to the same CFT as that of the physical edge, the two may differ by nonuniversal parameters such as the compactification radius. Other nonuniversal properties include effective fluxes, which change the boundary condition of the one-dimensional (1D) edge.

Our motivating questions are as follows: How does the ES decompose according to symmetry in 2D SPTs? How does this decomposition fit into the CFT? What are its universal properties, and how does the ES vary within a given SPT phase? Previous work by Scaffidi and Ringel exploring the emergent CFT in the ES of SPTs was limited to small system sizes [4]. It could, in principle, have performed a symmetry resolution, which does not require large systems. By contrast, distinguishing universal from nonuniversal properties upon continuous variation of the ground states, as we find, does require large system sizes.

In order to address these issues in this work, we develop an efficient numerical method [23,24] to calculate the ES of short-range entangled states in two dimensions. Our method is summarized in Fig. 1 and described in Sec. II. It uses a quantum circuit representation to construct gapped one-dimensional models that exhibit the same entanglement properties as the 2D SPTs in question. In particular, they allow us to extract the entanglement spectra of large systems and their symmetry resolution using tensor-network methods [25–28].

In Sec. III, we apply this approach to the Levin-Gu model [2] on an infinite cylinder with circumferences as large as $L = 150$. In agreement with previous studies of much smaller systems [4], we observe the spectrum of a CFT with central charge $c = 1$. Specifically, the ES can be organized in terms of primary states and their descendants. We find that all the
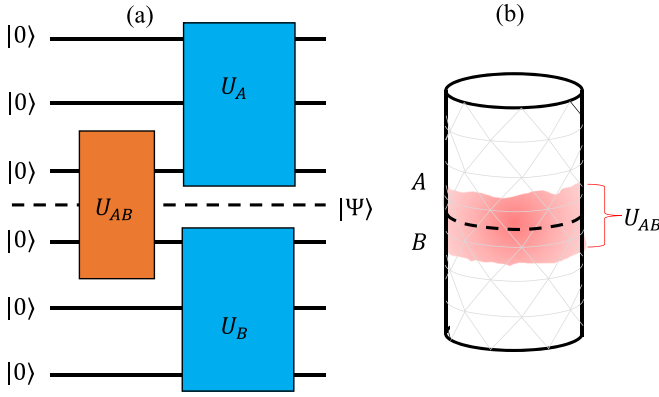
FIG. 1. Schematics of our method: (a) We analyze a state $|\Psi\rangle$ given as a quantum circuit representation as in Eq. (1). The entanglement between subsystems A and B is created by a unitary U_{AB} acting within a finite distance from the entanglement cut (dashed line). (b) We consider an SPT on a cylinder consisting of regions A and B.

descendant states have the same subsystem symmetry quantum numbers as the corresponding primary state. We also identify an unexpected subtlety in the ES of the Levin-Gu model: it distinguishes cylinders whose circumference is a multiple of three from all others. We attribute this effect to the lattice and show that it translates into a flux insertion of the corresponding CFT.

In Sec. IV, we apply our method to explore more generic states. We construct a continuous family of wave functions within one SPT phase using the framework of cohomological classification [29]. The ES of these states reveal a direct relation between so-called coboundary transformations and certain fluxes affecting the many-body SPT states.

In Sec. V, we further elaborate on the gapped one-dimensional models derived in Secs. III and IV. We demonstrate that they can be used to obtain the central charge of the SPT edge very efficiently without reference to ES. Restricting the edge Hamiltonian to terms that act within a single subsystem results in a critical chain that is described by the same CFT as the SPT edge. The central charge of such one-dimensional chains can be readily extracted from the scaling of the entanglement entropy, which satisfies the Calabrese-Cardy formula [30].

II. DIMENSIONAL REDUCTION AND TENSOR-NETWORK APPROACH

Before specifying to 2D, consider a d-dimensional space. The two subsystems A and B share a $(d-1)$-dimensional boundary $\partial A = \partial B$. By virtue of their finite depth circuit representation [31], any SPT state can be written as

$$|\Psi\rangle = U_A U_B U_{AB}|0\rangle. \tag{1}$$

Here $|0\rangle$ is a site-factorizable product state, i.e., the ground state of a trivial gapped Hamiltonian H_0 that is the sum over one-site operators. The unitaries U_A and U_B act only on subsystems A and B, respectively. U_{AB} acts in a $(d-1)$-dimensional region denoted C_{AB} extending a finite distance from ∂A; see Fig. 1(a). Consequently, the ES is fully encoded
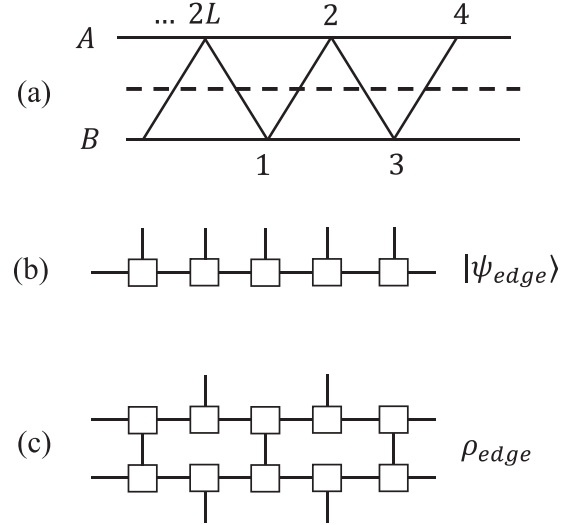
FIG. 2. (a) The resulting 1D edge Hamiltonian corresponding to Fig. 1(b) with the underlying triangular lattice is a zigzag chain containing both A (even) and B (odd) sites. (b) We construct a MPS of the ground state of H_{edge} living on A and B. (c) The reduced density matrix of subsystem A is constructed as an MPO by contracting the odd sites ($\in B$) of two copies of the MPS state.

in U_{AB}. Indeed, the reduced density matrix of region A is given by

$$\rho_A = \text{Tr}_B|\Psi\rangle\langle\Psi| = U_A\text{Tr}_B(U_{AB}|0\rangle\langle0|U_{AB}^\dagger)U_A^\dagger. \tag{2}$$

Up to the unitary transformation U_A, which does not affect the ES, ρ_A acts nontrivially only in the interface region C_{AB}. Consequently, the ES can be fully encoded by a state $|\psi_{\text{edge}}\rangle$ that lives only in C_{AB}. We define this edge state via $U_{AB}|0\rangle = |\psi_{\text{edge}}\rangle \otimes |0\rangle^{A \cup B \setminus C_{AB}}$ such that the operator

$$\rho_{\text{edge}} = \text{Tr}_B|\psi_{\text{edge}}\rangle\langle\psi_{\text{edge}}| \tag{3}$$

exhibits the same spectrum as ρ_A. The "edge density matrix" ρ_{edge} acts nontrivially only on a $(d-1)$-dimensional region within subsystem A. It is the central object in this paper, which we construct using tensor-network methods; see Fig. 2(c).

The presence of an onsite symmetry generated by $S = S_A \otimes S_B$ implies that $[\rho_A, S_A] = 0$. It follows that $[\rho_{\text{edge}}, U_A^\dagger S_A U_A] = 0$. As a result, the symmetry-resolved ES is obtained by diagonalizing ρ_{edge} simultaneously with the edge symmetry operator

$$S_{\text{edge}} = U_A^\dagger S_A U_A. \tag{4}$$

It is convenient to think of the pure state $|\psi_{\text{edge}}\rangle$ as the ground state of a local *edge Hamiltonian*

$$H_{\text{edge}} = U_{AB}H_0U_{AB}^\dagger, \tag{5}$$

which has the same (gapped) spectrum as H_0. H_{edge} acts on the support of C_{AB}, which contains the union of two adjacent $(d-1)$-dimensional regions in A and B. Accordingly, H_{edge} can be separated as

$$H_{\text{edge}} = H_A + H_B + H_{AB}. \tag{6}$$

We remark that, unlike the standard "entanglement Hamiltonian" H_E defined by $\rho_A = e^{-H_E}$, the edge Hamiltonian H_{edge}

acts on *both* subsystems. However, in Sec. V, we argue that H_E and H_A describe a CFT with the same universal properties dictated by the bulk SPT phase.

III. SYMMETRY-RESOLVED ES OF THE LEVIN-GU MODEL

Next, we focus on the paradigmatic 2D Levin-Gu model and demonstrate our method for the computation of the ES and its symmetry resolution. The Levin-Gu state admits a quantum circuit form [32]

$$|\Psi_{\text{LG}}\rangle = U_{CCZ}U_{CZ}U_Z|+\rangle, \tag{7}$$

where U_{CCZ}, U_{CZ}, and U_Z are, respectively, the products of CCZ, CZ, and Z gates acting on all triangles, edges, and vertices, and $|+\rangle$ is the ground state of $H_0 = -\sum_i X_i$. We consider a cylinder geometry as displayed in Fig. 1(b). Next, we use this quantum circuit form to derive a 1D Hamiltonian that encodes the ES of this 2D model, exemplifying the general prescription of Sec. II.

A. Gapped 1D edge Hamiltonian

The Levin-Gu state provides an explicit example of Eq. (1). In this case,

$$U_A = \prod_{\text{triangles}\in A} U_{CCZ}^{ijk} \prod_{\text{links}\in A} U_{CZ}^{ij} \prod_{\text{sites}\in A} U_Z^i, \tag{8}$$

and similarly for U_B. The triangles and links that connect the two subsystems identify the interface region C_{AB} as a zigzag chain with i even $\in A$ and i odd $\in B$; see Fig. 2(a). The corresponding entangling gates are

$$U_{AB} = \prod_i U_{CCZ}^{i-1,i,i+1} \prod_i U_{CZ}^{i,i+1} \equiv U_{AB}^{CCZ}U_{AB}^{CZ}. \tag{9}$$

The edge Hamiltonian of Eq. (5) is then given by

$$H_{\text{edge}} = U_{AB}H_0U_{AB}^\dagger = U_{AB}^{CCZ}H_{\text{cluster}}U_{AB}^{CCZ}, \tag{10}$$

where $H_{\text{cluster}} = U_{AB}^{CZ}H_0U_{AB}^{CZ} = -\sum_i Z_{i-1}X_iZ_{i+1}$ is the 1D cluster Hamiltonian. A more explicit form of H_{edge} is readily obtained by virtue of the identity

$$U_{CCZ}^{ijk}X_iU_{CCZ}^{ijk} = \tfrac{1}{2}X_i[I + Z_j + Z_k - Z_jZ_k]. \tag{11}$$

We thus obtain H_{edge} as a sum of tensor products of one-qubit operators,

$$\begin{aligned}
H_{\text{edge}} = \sum_i \frac{1}{4}X_i[&I - Z_{i-2} + Z_{i-1} + Z_{i+1} - Z_{i+2} \\
&+ Z_{i-2}Z_{i-1} + Z_{i-1}Z_{i+1} + Z_{i+1}Z_{i+2} \\
&- Z_{i-2}Z_{i+1} - Z_{i-1}Z_{i+2} - Z_{i-2}Z_{i+2} \\
&+ Z_{i-2}Z_{i-1}Z_{i+1} + Z_{i-2}Z_{i+1}Z_{i+2} \\
&+ Z_{i-2}Z_{i-1}Z_{i+2} + Z_{i-1}Z_{i+1}Z_{i+2} \\
&- Z_{i-2}Z_{i-1}Z_{i+1}Z_{i+2}]. \tag{12}
\end{aligned}$$

We construct a matrix product state (MPS) of the ground state of H_{edge}, denoted $|\psi_{\text{edge}}\rangle$ and depicted in Fig. 2(b), using the ITENSOR and JULIA libraries [33]. The ground state $|\psi_{\text{edge}}\rangle$ converges with bond dimension $\chi = 9$ for periodic boundary conditions. Subsequently, we construct the matrix product

operator (MPO) for ρ_{edge} by contracting the B sites of the outer product $|\psi_{\text{edge}}\rangle\langle\psi_{\text{edge}}|$; see Fig. 2(c). Finally, an excited-state density matrix renormalization group (DMRG) calculation on ρ_{edge} yields the ES.

B. Symmetry resolution

The $\mathbb{Z}_2$ symmetry operator of the Levin-Gu model is $X = \prod_i X_i$. To see that the Levin-Gu state is an eigenstate of X and determine its eigenvalue, we use the quantum circuit form [cf. Eq. (7)] along with the identities

$$\begin{aligned}
XZ_iX &= -Z_i, \\
XU_{CZ}^{ij}X &= -U_{CZ}^{ij}Z_iZ_j, \\
XU_{CCZ}^{ijk}X &= -U_{CCZ}^{ijk}U_{CZ}^{ij}U_{CZ}^{jk}U_{CZ}^{ki}Z_iZ_jZ_k. \tag{13}
\end{aligned}$$

The third identity implies, in particular, that

$$XU_{CCZ}X = (-1)^T U_{CCZ}, \tag{14}$$

where T is the number of triangles. The product over all triangles includes each link and each site an even number of times such that all Z and CZ factors cancel. Similarly, the product over all links includes each site an even number of times, and thus

$$XU_{CZ}X = (-1)^L U_{CZ}, \tag{15}$$

where L is the total number of links. It follows that

$$X|\Psi_{\text{LG}}\rangle = (-1)^{T+L+V}|\Psi_{\text{LG}}\rangle, \tag{16}$$

where V is the total number of vertices (i.e., sites). For a perfect triangular lattice without a boundary, $(-1)^{T+L+V} = 1$.

According to Eq. (4), the edge symmetry operator is given by $S_{\text{edge}}^{\text{LG}} = U_A^\dagger X_A U_A$, where $X_A = \prod_{i\in A} X_i$ and U_A is given by Eq. (8). Unlike the case of the full system, the product over all triangles in subsystem A involves the links along the edge only once. Consequently, commuting X_A across U_A using Eq. (13) produces uncanceled Z and CZ factors. Consequently, $S_{\text{edge}}^{\text{LG}}$ acts nontrivially near the edge and we write $U_A^\dagger X_A U_A = S_{\text{edge}}^{\text{LG}} \otimes \prod_{i\in A\setminus\partial A} X_i$. The first factor only acts on ∂A, which contains all even sites. It is given by

$$S_{\text{edge}}^{\text{LG}} = \prod_{i=\text{even}} X_i \prod_{i=\text{even}} U_{CZ}^{i,i+2}Z_i, \tag{17}$$

up to an additional overall factor $(-1)^{T_A+L_A+V_A} = 1$ accounting for the total number of triangles, links, and vertices in subsystem A. As we can see, in addition to the onsite factor $\prod_{i=\text{even}} X_i$, there is a nononsite factor [1]. The latter is the manifestation of the nontrivial SPT. In fact, it is this factor, which is classified [1] by the third cohomology group $\mathcal{H}^3(\mathbb{Z}_2, U(1)) = \mathbb{Z}_2$. One can rewrite the edge symmetry operator as

$$S_{\text{edge}}^{\text{LG}} = \prod_{j=\text{even}} X_j \prod_{j=\text{even}} e^{i\frac{\pi}{4}(Z_jZ_{j+2}-1)}, \tag{18}$$

which shows explicitly that the onsite and nononsite factors commute.

Having constructed the edge symmetry (18), we confirm that the eigenstates $|\psi_i\rangle$ of ρ_{edge} that we obtained from DMRG satisfy $S_{\text{edge}}^{\text{LG}}|\psi_i\rangle = s_i|\psi_i\rangle$, where $s_i = \pm 1$ is the symmetry eigenvalue.

Entanglement Hamiltonian

The above algorithm yields the eigenvalues λ_i of the reduced density matrix ρ_{edge}, from which we obtain a list of quasienergies $\xi_i = -\log \lambda_i$, being the eigenvalues of the entanglement Hamiltonian defined by $\rho_{\text{edge}} = e^{-H_E}$. According to the Li-Haldane conjecture [21], in topological systems, the latter displays the spectrum of a physical edge. In the present SPT, this spectrum is known to be a nonchiral free-boson CFT [1].

We match the list of quasienergies $\{\xi_0, \xi_1, \dots\}$ in increasing order to the form

$$\xi_i - \xi_0 = \frac{v}{L} \Delta_i, \tag{19}$$

where v is a free parameter corresponding to the velocity of the CFT, L is the circumference of the cylinder, and Δ_i are "scaling dimensions" of the CFT, as given below.

C. Entanglement spectrum for L divisible by 3

As discussed in detail in Appendix A, we can see that the numerically obtained eigenvalues of the entanglement Hamiltonian approximate the free-boson spectrum

$$\Delta(\ell, m, R) = \frac{\ell^2}{R^2} + \frac{R^2 m^2}{4} + \text{integers} \quad (\ell, m \in \mathbb{Z}), \tag{20}$$

with compactification radius $R = \sqrt{2}$. As reviewed in Appendix D, this spectrum can be viewed as an infinite set of primary states $|\ell, m\rangle$. Each of these generates an infinite tower of descendant states denoted in Eq. (20) by "integers."

The low-lying levels of this spectrum can already be seen to match this pattern in a short system of $L = 12$, as seen in Fig. 3. Results for longer systems, shown in Appendix A, confirm this pattern for higher-energy levels.

As required, each eigenvector of ρ_{edge} has a well-defined subsystem symmetry. We find that the corresponding quantum number is given by $s_i = (-1)^{\ell+m}$, as predicted from a field theory analysis [1,3]. In particular, all states generated by a given primary field inherit its symmetry properties. In Fig. 3, the symmetry eigenvalues $s_i = \pm 1$ are indicated in blue and red, respectively.

D. Entanglement spectrum for L nondivisible by 3

Our numerical results for lengths L that are not multiples of 3 follow a reproducible sequence different from Eq. (20). Instead, they approximate the pattern shown in Table I (cf. Appendix A). This sequence is captured by the modified free-boson spectrum

$$\Delta(\ell, m) = \frac{(\ell - \phi)^2 - \phi^2}{2} + \frac{m^2}{2} + \text{integers}, \tag{21}$$

with $\phi = \frac{1}{3}$, and the same symmetry resolution $s_i = (-1)^{\ell+m}$ as before. The parameter ϕ can be viewed as a flux threading the cylinder and affects the ground-state wave function like a many-body Aharonov-Bohm effect [3]. (In Appendix C we provide additional details that demonstrate this 3-periodicity using correlation functions.)
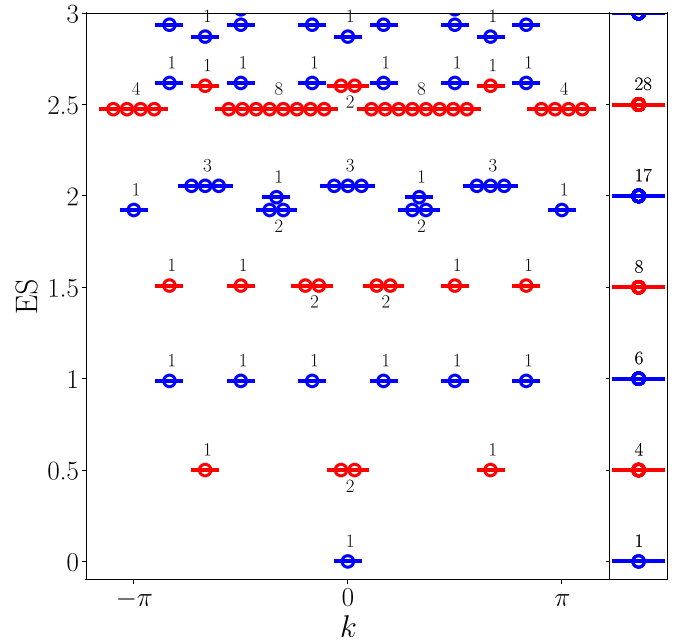
FIG. 3. Entanglement spectrum of the Levin-Gu model on a cylinder with circumference $L = 12$ and its symmetry resolution. The low-lying energy levels and their degeneracies match Eq. (20), with the second term "integers" being given by $\sum_{i>0} i(n_i + \bar{n}_i)$ with $n_i, \bar{n}_i \in \mathbb{N}$ being the ith integer ($i \geqslant 1$) excitation on top of the primary field denoted (ℓ, m). The right panel displays the ES levels and their degeneracy according to Eq. (20). The symmetry eigenvalue $s_i = \pm 1$ is denoted by blue and red, respectively.

E. Velocity of the edge CFT

So far we determined the spectra $\{\Delta_i\}$ by matching numerical results to a CFT pattern of levels with unit spacing between descendants. This removes any ambiguity in the values of Δ_1. We can now extract the velocity v from the ES. Indeed, we have $\xi_1 - \xi_0 = \frac{v}{L} \Delta_1$. This gives

$$\xi_1 - \xi_0 = \begin{cases} \frac{v}{2L}, & \text{for L divisible by 3} \\ \frac{v}{6L}, & \text{for L not divisible by 3.} \end{cases} \tag{22}$$

These two cases are plotted in Fig. 4. We thus obtain a value for the dimensionless velocity,

$$v \approx 11.023. \tag{23}$$

F. Symmetry equidecomposition in the thermodynamic limit

While the ES are different for the two symmetry sectors (blue vs red levels in Fig. 3), the total probabilities of the subsystem to be in either sector,

$$P_{\text{even/odd}} = \frac{\sum_{i \in \text{even/odd}} \lambda_i}{\sum_i \lambda_i}, \tag{24}$$

converge quickly to $\frac{1}{2}$ upon increasing L. The red curve in Fig. 5 shows $|P_{\text{even}} - P_{\text{even}}|$, which decays exponentially with system size.

As an attempt at an analytic description of the decay of $P_{\text{even}} - P_{\text{odd}}$ with L, we employ the CFT spectrum, although the latter only describes the low-lying levels, whereas the

TABLE I. ES for the Levin-Gu model on a cylinder with circumference L not divisible by 3 as described by Eq. (21). We display the degeneracy, quantum numbers (ℓ, m), and symmetry eigenvalues $s_i = (-1)^{\ell+m}$ of the low-lying states. The first descendants are denoted by $(\ell, m)'$. This spectrum is obtained in the thermodynamic limit from our numerical results in Appendix A. As our numerical methods are limited by computation time, the last row of the table has degeneracy marked by '?' due to this limited computation time.

Δ_i	Deg.	(ℓ, m)	s_i
0	1	(0,0)	1
1/6	1	(1,0)	−1
1/2	2	(0, ±1)	−1
2/3	2	(1,±1)	1
5/6	1	(−1,0)	−1
1	2	(0,0)′	1
7/6	2	(1,0)′	−1
4/3	3	(2,0), (−1,±1)	1
3/2	4	(0,±1)′	−1
5/3	4	...	1
11/6	4		−1
2	7		1
13/6	7		−1
7/3	?		1

probabilities $|P_{\text{even}} - P_{\text{even}}|$ presumably probe the entire spectrum. Nevertheless, from the CFT spectrum, we find

$$
P_{\text{even}} - P_{\text{odd}} = \frac{\sum_{\ell,m}(-1)^{\ell+m} e^{-\frac{v}{L}(\ell^2+m^2)}}{\sum_{\ell,m} e^{-\frac{v}{L}(\ell^2+m^2)}}
$$

$$
= \left(\frac{\theta_4 \left(e^{-\frac{v}{L}} \right)}{\theta_3 \left(e^{-\frac{v}{L}} \right)} \right)^2 \approx e^{-\frac{L\pi^2}{2v}}, \quad (25)
$$

where θ_i are Jacobi theta functions. In Fig. 5, we plot this difference for the velocity $v = 11.023$ (found in Sec. III E) as a dashed curve. The exponent does not quite match the numerical data, as expected. Curiously, the data can be fitted to Eq. (25) with another value of the velocity $v = 6.897$ (black curve).

IV. DEFORMED LG WAVE FUNCTIONS

The Levin-Gu wave function studied in the previous section lies within the unique nontrivial 2D SPT phase protected by the $\mathbb{Z}_2 = \{1, -1\}$ symmetry. In this section, we would like to explore how the ES varies within the SPT phase. We start with a convenient but inessential simplification of the parent LG state. Keeping only the CCZ gates in Eq. (7), we write

$$
|\Psi'_{LG}\rangle = U_{CCZ}|+\rangle. \quad (26)
$$

We study continuous deformations of this state given by

$$
|\Psi'_{LG}(\lambda)\rangle_{\text{cob}} = U_{\text{cob}}(\lambda)|\Psi'_{LG}\rangle, \quad (27)
$$

with

$$
U_{\text{cob}}(\lambda) = \prod_{\text{triangles}} \left(\frac{\lambda(Z_j, Z_k, 1)\lambda(Z_i, Z_j, 1)}{\lambda(Z_i, Z_k, 1)\lambda(Z_i, Z_j, Z_k)} \right)^{s_{ijk}}. \quad (28)
$$
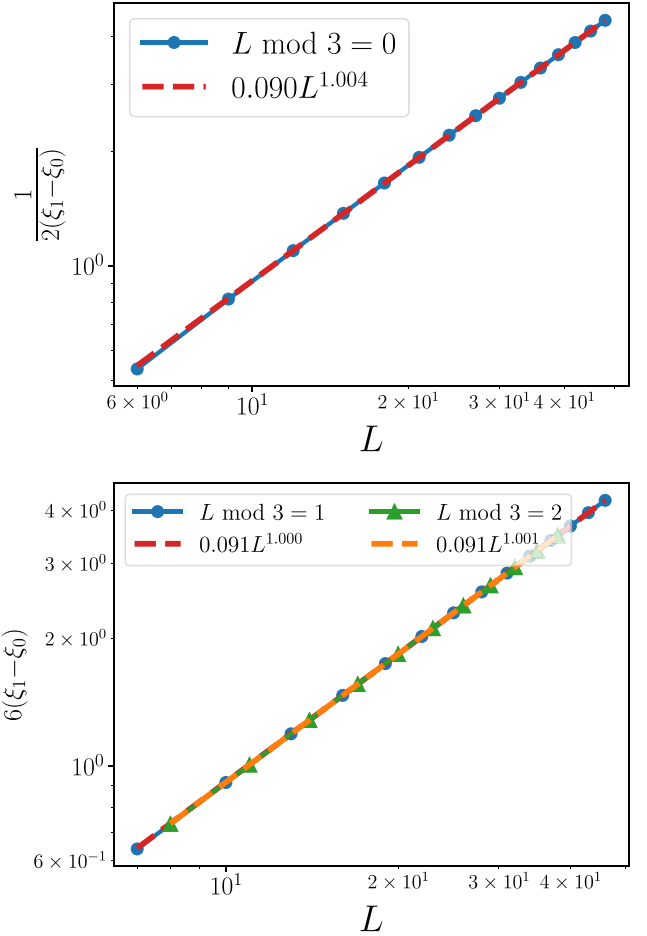
FIG. 4. Inverse of the finite-size gap in the quasienergy spectrum (i.e., eigenvalues of $-\log \rho_{\text{edge}}$) as a function of system size L. From Eq. (22), it allows to extract the velocity as in Eq. (23), which is obtained both for L divisible (upper panel) and not divisible (lower panel) by 3.

To define this transformation, one first enumerates all the vertices, and then denotes triangles by their ordered vertices $i < j < k$. Here, $s_{ijk} = \pm 1$ is the orientation of the triangle [29]. The U(1)-valued functions λ are invariant under the global symmetry, i.e., $\lambda(Z_i, Z_j, Z_k) = \lambda(-Z_i, -Z_j, -Z_k)$. Due to this symmetry, λ is parametrized by four independent phases. Each choice thereof yields a different wave function within the same nontrivial SPT phase since $U_{\text{cob}}(\lambda)$ is a local symmetric unitary transformation. The resulting wave function is a special case of more general cocycle wave functions, which are reviewed in Appendix E. In that context, $U_{\text{cob}}(\lambda)$ are referred to as coboundary transformations.

We can see that $U_{\text{cob}}(\lambda)$ can be incorporated into the quantum circuit form of Eq. (1) with

$$
U_{A(B)} = \prod_{\text{triangles}\in A(B)} U_{CCZ}^{ijk} \times U_{\text{cob}}^{A(B)}(\lambda), \quad (29)
$$

where

$$
U_{\text{cob}}^{A(B)}(\lambda) = \prod_{\text{triangles}\in A(B)} \left(\frac{\lambda(Z_j, Z_k, 1)\lambda(Z_i, Z_j, 1)}{\lambda(Z_i, Z_k, 1)\lambda(Z_i, Z_j, Z_k)} \right)^{s_{ijk}}. \quad (30)
$$
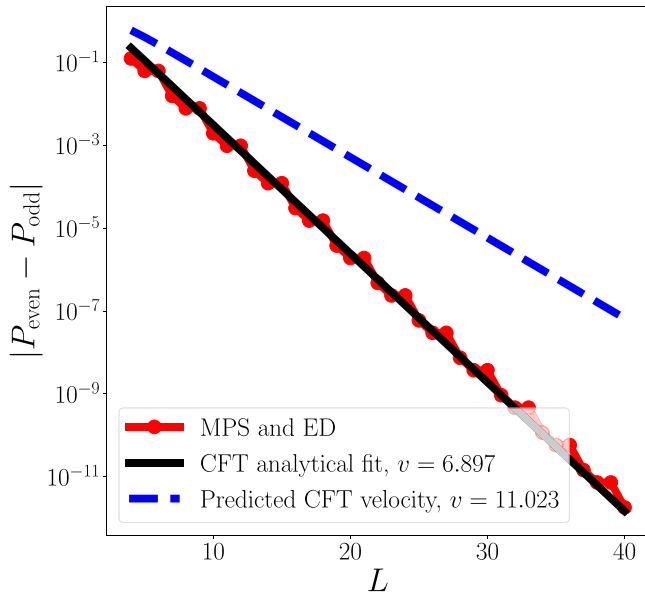
FIG. 5. Difference between the parity-resolved probabilities obtained from our tensor-network methods and confirmed using exact diagonalization for small systems, as a function of system size. Upon increasing L we obtain equipartition. We compare with the CFT prediction in Eq. (25) for two values of v.

Similarly, $U_{AB} = U_{AB}^{CCZ} U_{cob}^{AB}(\lambda)$, where

$$U_{cob}^{AB}(\lambda) = \prod_{\text{triangles} \in A\&B} \left(\frac{\lambda(Z_j, Z_k, 1)\lambda(Z_i, Z_j, 1)}{\lambda(Z_i, Z_k, 1)\lambda(Z_i, Z_j, Z_k)} \right)^{s_{ijk}}. \quad (31)$$

A. Coboundary transformations

To explore how the ES is affected by coboundary transformations, we follow a specific path through the four-dimensional parameter space of λ. Specifically, we take $\lambda(1, 1, 1) = \lambda(-1, 1, 1) = e^{i\theta}$ and $\lambda(1, -1, 1) = \lambda(-1, -1, 1) = 1$. This choice is arbitrary, and most other choices lead to the same phenomenology. Next, we apply our tensor-network methods to extract the ES of $|\Psi_{LG}'(\lambda)\rangle_{cob}$, together with its symmetry resolution. As derived in Appendix E, the edge symmetry operator (4) is affected by the transformation.

B. Results

We first construct the state $|+\rangle$, then apply U_{AB} to get the MPS state on the zigzag chain C_{AB}. Although the bond dimension may change with coboundary transformation, we find that, in our case, it is constant at $\chi = 9$. Subsequently, we construct ρ_{edge} as in Fig. 2(c), which doubles the bond due to the partial trace. Consequently, ρ_{edge} has the bond dimension 9^2.

For each value of θ, we obtain the low-lying eigenvalues and eigenvectors of the reduced density matrix. In Fig. 6, we plot the symmetry-resolved quasienergies for the first excited levels. Our results show how the ES evolves with θ. The obtained parabolic shapes motivate us to make an ansatz for the ES that corresponds to a flux insertion described by two additional parameters. Specifically, we expect the scaling di-
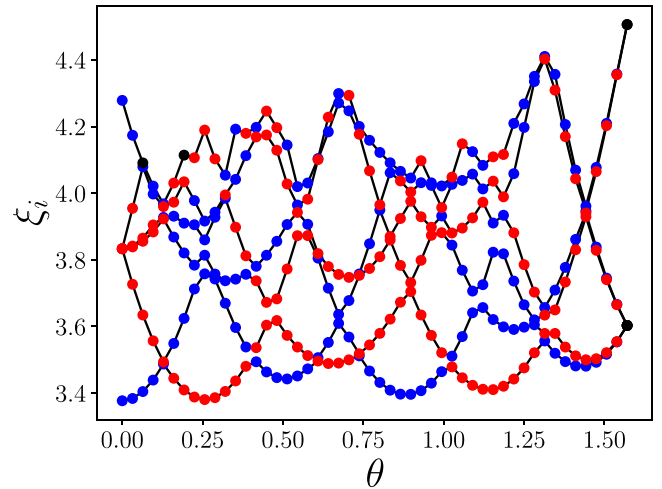
FIG. 6. Parity-resolved ES for the deformed Levin-Gu wave function (27) upon varying the variable θ controlling the coboundary transformations. We show the first six levels as obtained from DMRG calculation for $L = 12$. The symmetry eigenvalue $s = \pm 1$ is marked in blue and red, respectively.

mensions [Eq. (19) with a suitable choice of v] to match the shifted CFT spectrum

$$\Delta(\ell, m) = \frac{[\ell - \phi(\theta)]^2}{2} + \frac{[m - \varphi(\theta)]^2}{2} + \text{integers}$$
$$- \frac{(\phi(\theta))^2}{2} - \frac{(\varphi(\theta))^2}{2}, \quad (32)$$

where ϕ and φ are the flux parameters. To assess whether the data follow this formula, we numerically fix v, ϕ, and φ for each θ from the first four energy levels, i.e., three excitations $\xi_i - \xi_0$. Having fixed all the parameters in our ansatz, we compute four additional levels and find that they are correctly predicted by Eq. (32). In Fig. 7(a), we plot the scaled and shifted spectrum from the fit, for a small range of θ near $\theta = 0$. We see that the CFT indeed changes from no flux to a finite flux that depends on $\phi(\theta)$, $\varphi(\theta)$ as plotted in the inset. In Fig. 7(b), we focus on the vicinity of the point $\theta = \pi/2$, which displays a degeneracy between the symmetry sectors, and also corresponds to the form of Eq. (32) with $\phi = \varphi = \frac{1}{2}$. These findings corroborate our suggestion that the coboundary transformation mediates a flux insertion.

We note that the compactification radius of the CFT that captures the ES remains constant, independent of our transformations. There is *a priori* no reason for a fixed radius. Instead, this behavior implies that our coboundary transformations describe a limited set of transformations within the SPT phase. On the other hand, our finding of the continuously varying fluxes already suggests a nontrivial structure of the SPT phase as a manifold.

V. WIRE DECOMPOSITION OF H_{edge}

In the previous sections we saw that the ES is sensitive to nonuniversal details such as the system size modulo an integer or coboundary transformations. Consequently, identifying the gapless edge theory from the ES involves guesswork, which
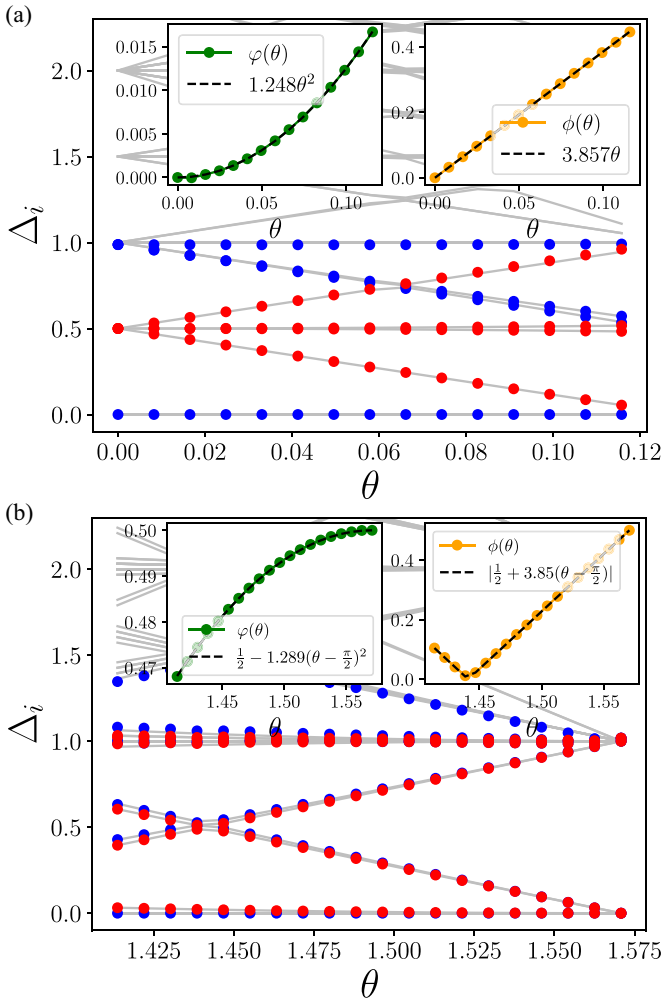
FIG. 7. The same ES as in Fig. 6, plotted in the form of the Δ_i defined in Eq. (19). In (a) we focus on the vicinity of $\theta = 0$, and in (b) we focus on the vicinity of $\theta = \pi/2$. The resulting levels match the CFT pattern (32). $\phi(\theta), \varphi(\theta)$ are calculated for each point and plotted in each inset. At $\theta = \pi/2$, we have $\phi(\pi/2) = \varphi(\pi/2) = \frac{1}{2}$ corresponding to a fourfold-degenerate lowest level. See Appendix F regarding the generation of the fits.

may sometimes be difficult to achieve. In this section, we provide an algorithm to identify the gapless theory based on the gapped edge Hamiltonian H_{edge}. The following decomposition is similar to field-theoretical wire constructions of fractional quantum Hall states [34–37], SPTs [38], or other spin liquids [39–41].

We decompose the 1D edge Hamiltonian as

$$H_{\text{edge}} = H_A + H_B + H_{AB}, \tag{33}$$

where $H_{A(B)}$ acts only within $A(B)$, and H_{AB} couples A and B. Based on the Li-Haldane conjecture [21] it was argued [42–44] that the ES between the legs of a two-leg ladder resembles the actual energy spectrum of each decoupled leg. Following this relationship in reverse, we suggest to infer the nature of the gapless theory describing the ES from the isolated chain H_A.

We remark that the study of H_A reveals a number of interesting properties, such as a period 3 modulation of correlation
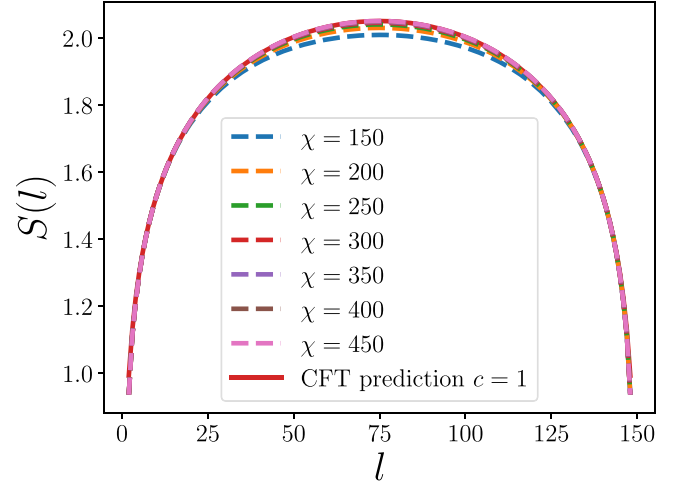
FIG. 8. Entanglement entropy for the ground state of H_A^{LG} in Eq. (34) as a function of subsystem size l obtained from a MPS with system size $L = 150$ and varying bond dimension χ. The numerical result converges to the CFT result (35) with central charge $c = 1$.

functions and a corresponding threefold dependence on L of the finite-size spectrum. Thus, the difference of the ES found in Sec. III depending on whether $L/3$ is a integer or not has its origin already on the level of a single chain. Additionally, the model H_A has the nice property that finite-size properties converge very quickly to the infinite-size limit. Below, we show results for the entanglement entropy of this 1D model.

A. Spectrum of H_A of the Levin-Gu model

For the Levin-Gu model, the Hamiltonian H_A^{LG} is given in Eq. (12),

$$H_A^{\text{LG}} = \sum_{i=1}^{L} [(Z_{i-1}X_iZ_{i+1} - X_i) + (Z_{i-1}X_i + X_iZ_{i+1})], \tag{34}$$

where here we only focus on subsystem A, so we label its sites by integer i (rather than even integer). The decomposition of H_A^{LG} into two terms is inessential for our purposes; it refers to the fact that, individually, each term is easily seen to yield a gapless spectrum. The fate of the full Hamiltonian is not readily apparent, and we determine it numerically. Specifically, by exploring the scaling of its ground-state entanglement entropy, we show that H_A^{LG} is gapless and extract the central charge c of its field theory. In Fig. 8, we plot the entanglement entropy S of a bipartition of this 1D chain of length L as a function of subsystem size l. The numerical values are compared with the analytical CFT expression [30]

$$S(l) = \frac{c}{3} \log\left(\frac{L}{\pi} \sin\left[\frac{\pi l}{L}\right]\right) + \kappa, \tag{35}$$

where c is the central charge and κ is a nonuniversal constant. We find that $c = 1$ agrees very well with the numerical data.

B. Robustness of the central charge upon coboundary transformations

The central charge $c = 1$ is expected to describe the edge theory for the entire SPT phase. We now consider the 1D
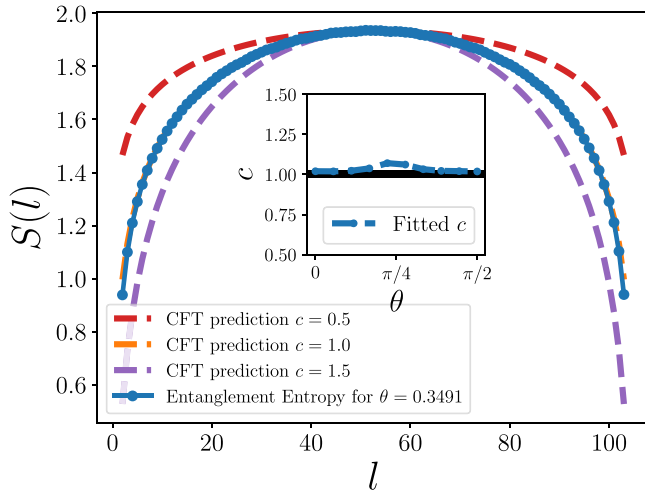
FIG. 9. Entanglement entropy, as in Fig. 8, but for the ground state of Eq. (36), describing the wire decomposition of the deformed Levin-Gu state, as parametrized by θ, and also *symmetry resolved* to a definite parity sector. In the main panel we consider the ground state of H_A for a specific arbitrary point, $\theta \approx 0.3491$, and compare it with the CFT predictions for different central charges. We see that it matches $c = 1$, as expected. In the inset, we plot the fit of the central charge for varying θ, yielding $c \approx 1$ for all values of θ up to a maximal deviation of $\sim 7\%$. The fit is generated from H_A^{θ} of a subsystem of size $L = 105$ and $\chi = 4L = 420$.

edge Hamiltonian whose ground state is $|\Psi'_{\text{LG}}(\lambda)\rangle_{\text{cob}}$. Our aim is to show that c is independent of λ. The explicit form of this Hamiltonian, and its decomposition as in Eq. (6), is cumbersome. In practice, we simply have

$$H_A(\lambda) = \text{Tr}_B(U_{AB} H_0 U_{AB}^{\dagger}), \qquad (36)$$

where U_{AB} depends on λ as given in Eq. (31). Using our tensor-network methods, we perform the partial trace over B for the MPO representing $H = U_{AB} H_0 U_{AB}^{\dagger}$ [similar to Fig. 2(c)] to obtain an MPO representing H_A. We find its ground state and compute the entanglement entropy using DMRG.

In Fig. 9, we show that coboundary transformations indeed preserve a good fit with $c = 1$ for generic values of θ, which parametrizes our coboundary transformation.

VI. SUMMARY

1D SPTs display degeneracies in their ES [17]. When performing a symmetry resolution of the ES, these degeneracies reflect an equidecomposition of the entanglement eigenvalues among different symmetry sectors [14]. Here, we showed that the gapless ES of 2D SPTs also have a natural symmetry decomposition. The gapless spectrum is described by a CFT and can be divided into towers of states which are descendants of primary fields. The symmetry quantum numbers are determined by the corresponding primary states.

To demonstrate these claims explicitly for large systems on concrete models, we developed tensor-network-based methods. Starting from a d-dimensional tensor network of a short-range entangled state, we reduced the computation of the ES to a $(d - 1)$-dimensional problem. For $d = 2$, on which

we focused, we ended up with effective 1D calculations that can be dealt with efficiently.

Our construction parallels the wire construction of topologically ordered phases, like the 2D fractional quantum Hall effect (FQHE). By breaking the 2D problem into coupled wires, the ES is universally stored in this interwire coupling [22]. Yet, the wire construction of nonchiral SPT order [38] has its unique features. In contrast to the wire construction of the chiral topological ordered case, in our nonchiral case we showed that the spectrum of the decoupled wires itself reflects the spectrum of the edge or, equivalently [21], of the ES.

In the context of the FQHE and similar states, the wire construction allowed to explicitly construct effective quasi-1D synthetic realizations, e.g., using cold atoms [45–49], which could be much easier to realize compared to their full 2D versions. In this sense, our 1D tensor-network approach gives explicit quasi-1D models for 2D SPT order. This allows realizations of such states and explorations of their symmetry-resolved entanglement, e.g., on a small quantum computer, hence generalizing many existing realizations of 1D topological states, such as the cluster state [14].

APPENDIX A: NUMERICAL RESULTS FOR THE LEVIN-GU MODEL

In this Appendix, we present numerical results for the ES of the Levin-Gu model calculated using the methods of Secs. II and III. The lists of numerical results in Tables II and III contain two columns for each L. The left column shows the bare eigenvalues λ_i of the ES. Results for small systems confirmed by exact diagonalization are denoted by (ED). The second column of Δ_i's denoted "CFT" is obtained from the first column by using Eq. (19), by fixing v such that $\Delta_1 = \frac{1}{2}$ for L being a multiple of 3 ($L = 12, 18, 24, 30$), or $\Delta_1 = \frac{1}{6}$ for L not being a multiple of 3 ($L = 14, 17, 20$).

We can see that for L being a multiple of 3, the shifted and rescaled spectrum is a good approximation of Eq. (20), and for L's that are not multiples of 3 the ES follows the pattern in Eq. (21).

APPENDIX B: EXACT DIAGONALIZATION OF THE REDUCED DENSITY MATRIX FOR THE LEVIN-GU MODEL

1. Eigenvalues of ρ_A

Consider the ground state of Levin-Gu model $|\psi\rangle = \sum_{s_i \in \{0,1\}^S} U_{CCZ} U_{CZ} U_Z |s_i\rangle$, where S is the number of spins in

TABLE II. The largest eigenvalues of the ES for L that is a multiple of 3 obtained numerically mostly by using MPS methods described in the text. Blank lines separate degenerate eigenvalues to ease reading. The result of $L = 12$ is a result of ED to provide a comparison of the two methods. The results are scaled in the CFT column to match the CFT spectrum described in the text.

$L = 12$ (ED)	CFT	$L = 18$	CFT
0.03415	0	0.005927	0
0.02164	0.5	0.004377	0.5
0.02164	0.5	0.004377	0.500038
0.02164	0.500004	0.004376	0.500224
0.02164	0.500006	0.004376	0.500332
0.01386	0.987772	0.003241	0.995632
0.01386	0.987772	0.003241	0.995650
0.01386	0.987774	0.003241	0.995566
0.01386	0.987774	0.003240	0.996146
0.01386	0.987774	0.003241	0.995580
0.01386	0.987774	0.003240	0.996040
0.00861	1.509386	0.002376	1.507274
$L = 24$	CFT	$L = 30$	CFT
0.00104116	0	0.00018325	0
0.00082965	0.5	0.00015283	0.5
0.00082933	0.500836	0.00015283	0.500048
0.00082957	0.500206	0.00015234	0.508910
0.00082866	0.502614	0.00015230	0.509600
0.00066105	1.000170	0.00012711	1.007720
0.00066145	0.998830	0.00012668	1.017110
0.00066110	1.000012	0.00012707	1.008628
0.00066109	1.000022	0.00012720	1.005916
0.00066051	1.001982	0.00012646	1.021908
0.00066053	1.001900	0.00012647	1.021750
0.00052246	1.518194	0.00010430	1.552650

TABLE III. The largest eigenvalues of the ES for L that is not a multiple of 3 obtained numerically mostly by using MPS methods described in the text. The result of $L = 17$ is a result of ED to provide a comparison of the two methods. The results are scaled in the CFT column to match the CFT spectrum described in the text.

$L = 14$	CFT	$L = 17$ (ED)	CFT
0.018205	0	0.007651817	0
0.015989	0.166666	0.006876625	0.166666
0.012325	0.500964	0.005552095	0.500502
0.012324	0.501028	0.005552092	0.500503
0.010847	0.665022	0.004995132	0.665447
0.010847	0.665024	0.004995132	0.665447
0.009456	0.841195	0.004470445	0.838606
0.00837	0.997875	0.004036603	0.997891
0.008375	0.997212	0.004036602	0.997891
0.007323	1.169509	0.003619472	1.168084
0.007321	1.169927	0.00361947	1.168085
0.006485	1.325660	0.003264707	1.329045
0.006483	1.325973	0.003264706	1.329045
0.006338	1.355135	0.003225258	1.348014
0.005654	1.501629	0.002925212	1.500374
0.005655	1.501508	0.002925211	1.500374
$L = 20$	CFT	$L = 31$	CFT
0.00321689	0	0.000134971	0
0.00293769	0.166666	0.000127297	0.166666
0.00244834	0.501161	0.000113078	0.503877
0.00244611	0.502827	0.000113039	0.504854
0.00223668	0.667140	0.000106617	0.671371
0.00223563	0.667999	0.000106650	0.670488
0.00203912	0.836892	0.000100668	0.834815
0.00185763	1.008016	0.0000941542	1.025287
0.0018588	1.006858	0.0000942865	1.021286
0.00169606	1.175047	0.0000887601	1.193246
0.0016941	1.177177	0.0000888650	1.189886
0.00155797	1.330952	0.0000843737	1.337537
0.00155589	1.333401	0.0000843754	1.337478
0.00154704	1.343873	0.0000843887	1.337029
0.00141089	1.512986	0.0000789565	1.526459
0.00141119	1.512589	0.0000788018	1.532042

the system and U_{CCZ}, U_{CZ}, U_Z are as defined in the main text. Here we focus on the reduced density matrix for subsystem A, which is obtained by partial trace over the complement of A, which we denote as B. Its eigenvalues give the ES of the system. We will show how we obtain the partial trace efficiently using numerical methods.

Let us now focus on the Hamiltonian dynamics of the resulting edge. The ground state is

$$|\Psi_{LG}\rangle = \sum_{s_A, s_B, s_{AB}} U_{CCZ}(s_A, s_B, s_{AB}) U_{CZ}(s_A, s_B, s_{AB})$$
$$\times U_Z(s_A, s_B, s_{AB}) |s_A, s_B, s_{AB}\rangle . \quad (B1)$$

As in the main text, by splitting the U's pieces acting uniquely on A, B or on the boundary AB, we are able to ignore and cancel the A, B bulk parts, respectively. Hence, we have that the reduced density matrix entries are

$$\rho_{s_A, s'_A} = \sum_{s_B} U_{CCZ}^{AB}(s_A, s_B) U_{CCZ}^{AB}(s'_A, s_B)$$
$$\times U_{CZ}^{AB}(s_A, s_B) U_{CZ}^{AB}(s'_A, s_B), \quad (B2)$$

where U^{AB} are the unitaries that act on both subsystems A and B, $s_{A,B}$ are binary strings representing the spins on the boundaries of A, B, and we use the standard (Z) basis of spins.

The structure of ρ_A further decomposes into the product of matrix M and its Hermitian conjugate $M^\dagger$. Let us define $M = \sum_{s_A, s_B} U_{CCZ}^{AB}(s_A, s_B) U_{CZ}^{AB}(s_A, s_B) |s_A\rangle \langle s_B|$ as the matrix representing the action of the unitaries on the edge qubits for a specific choice of s_A and s_B. It is then clear that $\rho_A = MM^\dagger$, as the summation over the B edge spins is performed by the matrix multiplication, and the dagger matches the B part to reproduce ρ_A. Hence, to obtain the eigenvalues of ρ_A, we only need to compute M, which is more efficient than computing ρ_A.

Moreover, we deduce the eigenvalues of ρ_A from the matrix M. We verified numerically that $[M, M^\dagger] = 0$ (we have yet to have an analytical proof for this). Hence, by the spectral theorem the eigenvalues of ρ_A are simply the absolute value squared of the M eigenvalues. The terms in M are much easier to compute, and thus our method overall is about 2^L times faster than the naive way of calculating ρ_A as we do not sum over s_B, where $2L$ is the number of spins on the boundaries.

2. Symmetry resolution of ρ_A

In order to obtain the symmetry-resolved entanglement, one needs to calculate how the symmetry acts in the Gu-Levin basis. Gu-Levin basis $|\sigma\rangle$ is defined as the summation over all configurations in A with a specific configuration σ for the boundary spins, where each such configuration gets a sign $(-1)^{N_A}$ where N_A is the number of domain walls calculated with $|\uparrow\rangle$ ghost spins on the boundary. We conjecture (the proof can be done by induction) that $X_A |\sigma\rangle = (-1)^{D+1} |\bar{\sigma}\rangle$ where D is the number of domain walls on the boundary of A divided by 2. Therefore, we see that the symmetry acts nontrivially on the boundary, as we expect for SPT phases.

To obtain the symmetry-resolved blocks of ρ_A, we apply the projection $\frac{I \pm X_A}{2}$ on both sides of ρ_A. This is done by computing $\rho_A = AA^\dagger$ and then computing $\frac{I \pm X_A}{2} \rho_A \frac{I \pm X_A}{2} = \frac{1}{4}[\rho_A + X_A \rho_A X_A \pm \rho_A X_A \pm X_A \rho_A]$ element by element using the action of X_A in the Levin-Gu basis. Similarly, one can get the momentum k from the translation symmetry T_A with similar projections. Therefore, the ES is constructed with its symmetry resolution using ED for systems up to length $L = 12$.

APPENDIX C: CORRELATIONS IN H_A

In this Appendix, we further explore manifestations of the threefold periodicity. In the main text we argued that the ES is described by a $c = 1$ CFT for all system sizes L, but with different fluxes for $L = 3n$ or $L \neq 3n$. Here, we explore the ground-state properties of the Hamiltonian H_A derived from Eq. (34) for the Levin-Gu model to understand the origin of this threefold periodicity.

The model H_A belongs to the family of Hamiltonians

$$H = -\left[\sum_i \cos(\alpha)(X_i - Z_{i-1}X_iZ_{i+1}) \right.$$
$$\left. + \sin(\alpha)(-Z_{i-1}X_i - X_iZ_{i+1}) \right], \qquad \text{(C1)}$$

which interpolates between gapless models. For $\alpha = 0$ or $\alpha = \frac{\pi}{2}$, this Hamiltonian maps onto an XY model. Consequently, these cases are described by $c = 1$ CFTs. The point $\alpha = \frac{\pi}{4}$ recovers Eq. (34). It corresponds to the Levin-Gu case, which is also a $c = 1$ CFT, as we have seen in Sec. V A. We note that this 1D model has an interesting phase diagram as a function of α that may be worth exploring in detail. For our purposes, we now focus on the Levin-Gu case and show that the ground state of this Hamiltonian has period-three features in its correlation functions.

We study the correlation functions $\langle \sigma_i \sigma'_j \rangle - \langle \sigma_i \rangle \langle \sigma'_j \rangle$, where $\sigma, \sigma' = X, Y, Z$ are the different Pauli matrices. To obtain these correlations, we use the MPS procedure. References [27,50,51] showed that the MPS always exhibits an exponential damping of the correlation functions, which may not approximate ground states with algebraic correlations (e.g., $|i - j|^{-\alpha}$). Hence, the MPS method introduces exponential errors in the large $|i - j|$ regime. These errors are circumvented by increasing the bond dimension χ. Additionally, as we simulate only finite systems, we have finite-size effects.
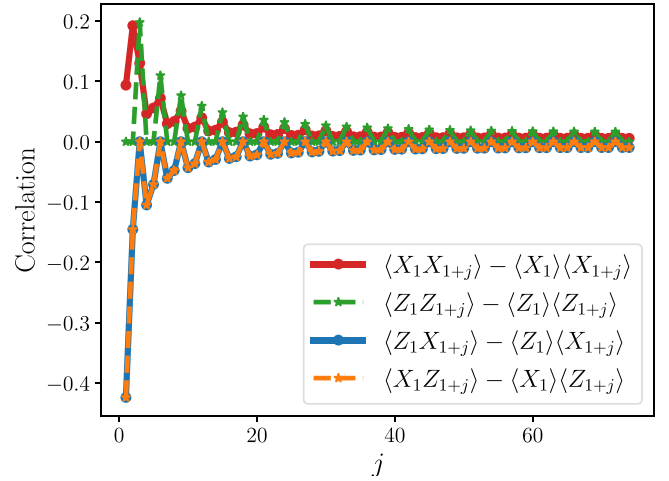
FIG. 10. Different correlation functions for the ground state of the Hamiltonian H_A^{LG} for system size $L = 150$. All these correlations exhibit threefold periodicity.

In Fig. 10 we show $\langle \sigma_1 \sigma'_{1+j} \rangle - \langle \sigma'_1 \rangle \langle \sigma'_{1+j} \rangle$ as a function of j, for a system of size $L = 150$ and bond dimension $\chi = 450$. The threefold periodicity is evident in all four correlation functions. This behavior explains the origin of the same periodicity seen in the ES in the main text as function of L.

To better understand these correlation functions, we separately analyze each of the three components with threefold periodicity. In Fig. 11, we show them on a logarithmic scale. All nonzero correlation functions are consistent with a power-law decay. Some of the correlation function yields exponents close to unity, but others follow more unusual power laws with exponents ≈ 0.85.

APPENDIX D: FIELD THEORY

References [1,3] provide a field-theory description of the physical edge of an SPT together with the action of the symmetry. We will accommodate the results of the symmetry-resolved entanglement within this field theory.

The field theory is constructed naturally by generalizing the $\mathbb{Z}_2$ symmetry to a $\mathbb{Z}_N$ symmetry. The edge theory consists of a pair of fields $\phi_I(x)$ ($I = 1, 2$), where $\frac{1}{2\pi} \partial_x \phi_2(x)$ is the canonical momentum conjugate to $\phi_1(x)$. The $\mathbb{Z}_N$ symmetry in the pth phase ($p = 0, 1, \ldots, N - 1$) of $\mathcal{H}^3(\mathbb{Z}_N, U(1)) = \mathbb{Z}_N$ is

$$S_{\mathrm{edge}}^{(p)} = e^{\frac{i}{N}\left(\int_0^L dx\, \partial_x \phi_2 + p \int_0^L dx\, \partial_x \phi_1 \right)}. \qquad \text{(D1)}$$

We can recognize the product of two commuting factors, as in Eq. (18).

With the mode expansion

$$\phi_I(x) = \phi_{0I} + K_{IJ}^{-1} P_{\phi J} \frac{2\pi}{L} x + i \sum_{n \neq 0} \frac{1}{n} \alpha_{I,n} e^{-inx\frac{2\pi}{L}}, \qquad \text{(D2)}$$

where $[\phi_{0I}, P_{\phi J}] = i\delta_{IJ}$, $[\alpha_{I,n}, \alpha_{J,m}] = nK_{IJ}^{-1}\delta_{n,-m}$, one obtains the canonical quantized fields with the commutation relations

$$[\phi_I(x_1), K_{I'J} \partial_x \phi_J(x_2)] = 2\pi i \delta_{II'} \delta(x_1 - x_2), \qquad \text{(D3)}$$
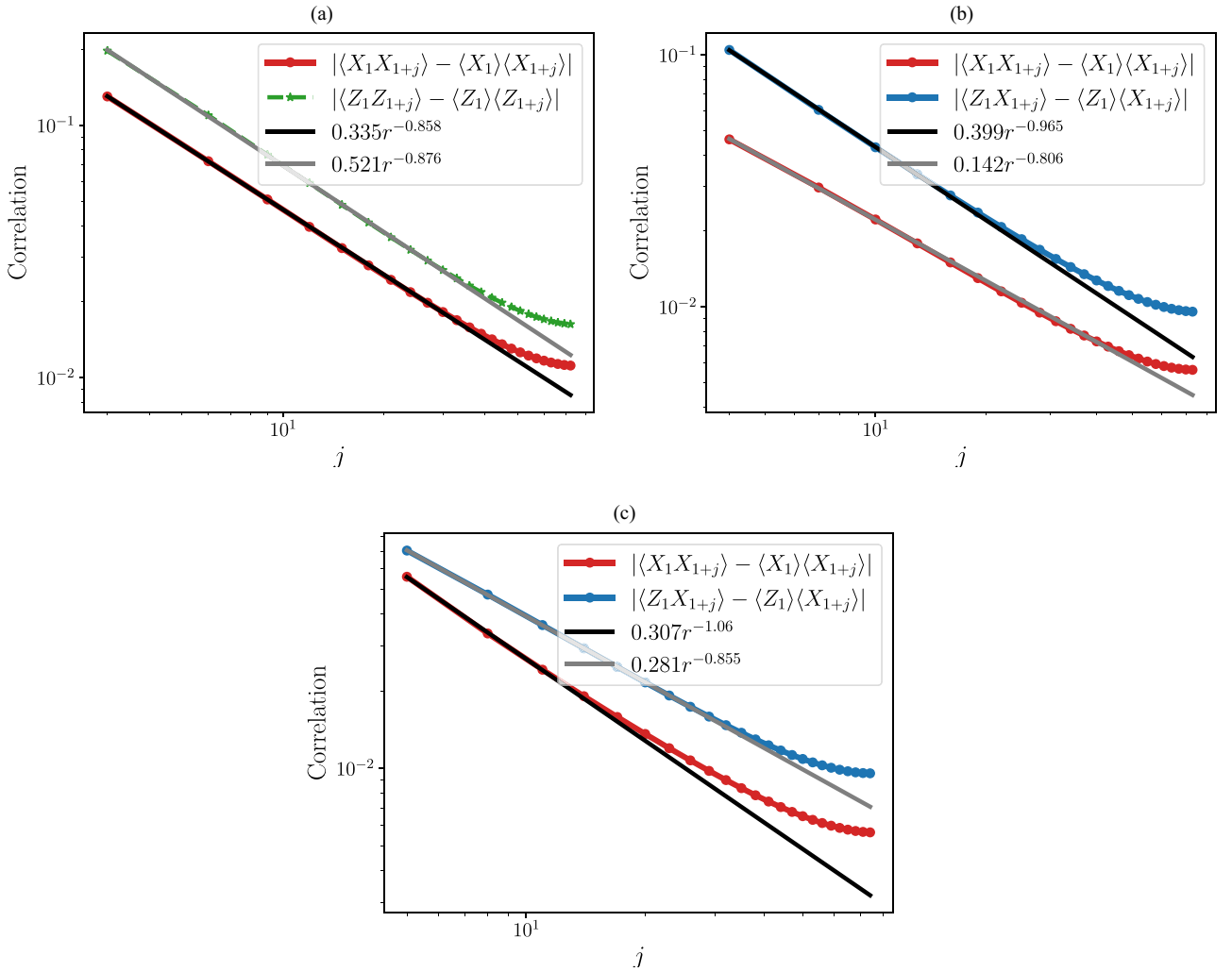
FIG. 11. Power-law fits for selected correlations on log-log scale for the Levin-Gu case for a system size $L = 150$ and bond dimension $\chi = 450$. The fits (a)–(c) are generated from the j modulo $3 = 0, 1, 2$ points, respectively. The correlations match power laws.

where $K_{IJ} = (\sigma^x)_{IJ}$. The winding numbers $(P_{\phi 1}, P_{\phi 2})$ are integers denoted (l, m) and determine the edge symmetry $S_{\text{edge}}^{(p)} = e^{\frac{2\pi i}{N}(P_{\phi 2} + p P_{\phi 1})}$.

Under inversion of the edge coordinate $\phi_1 \rightarrow \phi_1$ and $\phi_2 \rightarrow -\phi_2$, allowing us to define right- and left-moving fields $\phi_{R,L} = \phi_1 \pm \phi_2$. Based on this symmetry, the most general quadratic Hamiltonian can be written in terms of a pair of parameters as

$$H = v \int \frac{dx}{(2\pi)^2} \left(\frac{1}{R^2} (\partial_x \phi_1)^2 + \frac{R^2}{4} (\partial_x \phi_2)^2 \right). \quad \text{(D4)}$$

Substituting the mode expansion yields

$$H = \frac{v}{L} \left[\left(\frac{\ell^2}{R^2} + \frac{m^2 R^2}{4} \right) + \sum_{n>0} n(a_n^\dagger a_n + b_n^\dagger b_n) \right], \quad \text{(D5)}$$

where the bosonic creation and annihilation operators a_n, b_n with canonical commutation relations are related to the $\alpha_{I,n}$ by a rescaling and Bogoliubov transformation. The primary edge states are labeled by (ℓ, m) and have the symmetry $S_{\text{edge}}^{(p)} = e^{\frac{2\pi i}{N}(m + p\ell)}$. One obtains infinite towers of states above these states generated by creating bosonic excitations.

APPENDIX E: 2D COCYCLE WAVE FUNCTIONS

In this Appendix, we apply our tensor-network methods for 2D cocycle wave functions. In contrast to the main text, we denote the group elements by $\mathbb{Z}_2 = \{0, 1\}$, with "0" representing the identity, to match standard notation in the literature [29]. The Gu-Levin $\mathbb{Z}_2$ wave function studied in the previous section lies within the unique nontrivial 2D SPT phase. It corresponds to a specific cocycle wave function. Within the cohomological formalism, coboundary transformations allow us to move in the SPT phase and explore how the ES varies within the SPT phase.

1. Cocycle wave functions

We begin by briefly reviewing the construction of the cocycle wave function [29]. Consider a 2D triangular lattice on the 2-sphere. The Hilbert space at each site is spanned by the symmetry group elements $|g\rangle$, $g \in G = \mathbb{Z}_2 = \{0, 1\}$ (with
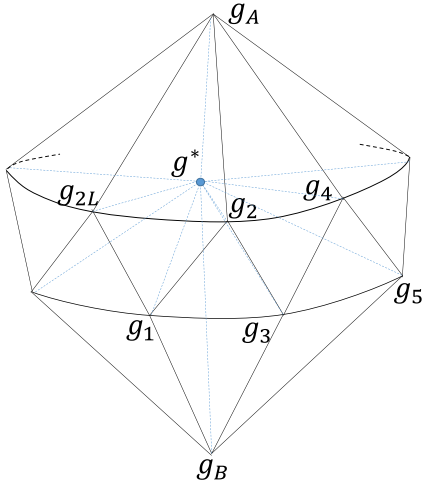
FIG. 12. The triangulated 3D lattice used to construct the cocycle wave function. Region A corresponds to the top part of the 2D surface, with one site in the "bulk" g_A and L sites at the boundary. Similarly, subsystem B contains only one site in the bulk g_B. The 3D lattice has one site in its interior, denoted g^*.

an obvious generalization to $\mathbb{Z}_N$). The onsite action of the symmetry is $S_h|g\rangle = |hg\rangle$ with $h \in G$. The trivial symmetric ground state is given by $|+\rangle \equiv \otimes_i (\frac{1}{\sqrt{|G|}} \sum_g |g\rangle)$.

The ideal SPT wave function is constructed as follows. We are interested in placing an SPT on the 2-sphere. In order to write its wave function we consider the 2-sphere as the boundary of a 3-ball. We minimally triangulate this $(d + 1)$-dimensional space; to be specific we consider Fig. 12 [see Fig. 6(a) in Ref. [16]]. Here, we place only one site, $g^* = 0$, in the interior of the 3-ball. The remaining sites are located on the 2-sphere, and the corresponding states are denoted $\{g_i\}$. Region A consists of the upper hemisphere and includes $i = \text{even} = 2, \ldots, 2L$ on the zigzag chain in Fig. 1(c) and one extra site g_A in the bulk of A. Similarly, region B in the lower hemisphere includes the sites with odd i and one extra site in the bulk of B corresponding to a state g_B.

The SPT state is written as $|\Psi\rangle = \sum_{\{g_i\}} \psi(\{g_i\})|\{g_i\}\rangle$, where the wave function $\psi(\{g_i\})$ is constructed using 3-cocycles, which reside on the tetrahedra, as explained next.

2. Cochains, cocycles, and coboundaries

3-cochains, $\nu_3(g_0, g_1, g_2, g_3)$, are U(1)-valued functions of $d + 2 = 4$ G-valued variables g_0, g_1, g_2, g_3, $|\nu_3(g_0, g_1, g_2, g_3)| = 1$, which satisfy $\nu_3(g_0, g_1, g_2, g_3) = \nu_3(hg_0, hg_1, hg_2, hg_3)$ for any $h \in G$.

3-cocycles are special cochains satisfying $\prod_{i=0}^{4} \nu_3^{(-1)^i}(g_0, \ldots, g_{i-1}, g_{i+1}, g_4) = 1$, namely,

$$\frac{\nu_3(g_1, g_2, g_3, g_4)\nu_3(g_0, g_1, g_3, g_4)\nu_3(g_0, g_1, g_2, g_3)}{\nu_3(g_0, g_2, g_3, g_4)\nu_3(g_0, g_1, g_2, g_4)} = 1.$$

A 3-coboundary is a special 3-cocycle that is a "derivative" of a 2-cochain $\lambda_2(g_0, g_1, g_2)$,

$$(d\lambda_2)(g_0, g_1, g_2, g_3) = \frac{\lambda_2(g_1, g_2, g_3)\lambda_2(g_0, g_1, g_3)}{\lambda_2(g_0, g_2, g_3)\lambda_2(g_0, g_1, g_2)}. \quad \text{(E1)}$$

It automatically satisfies the cocycle condition.

In our construction in Fig. 12, all tetrahedra consist of four vertices, containing g_i, g_j, g_k, which reside on the 2-sphere, and g^* which resides in the interior of the 3-ball. Each 3-cocycle ν_3 corresponds to a wave function

$$\psi(\{g_i\}) = N \prod_{ijk \in \Delta} \nu_3^{s_{ijk}}(g_i, g_j, g_k, g^*), \quad \text{(E2)}$$

where g_i, g_j, g_k, g^* run over the vertices of all tetrahedra in Fig. 12. Here, $s_{ijk} = \pm 1$ is determined by the clockwise or anticlockwise chirality of the triangle dictated by increasing order $i < j < k$. Here g^* can be chosen arbitrarily [29] to be $g^* = 0$.

The cochain condition guarantees that $|\Psi\rangle = \sum_{\{g_i\}} |\{g_i\}\rangle$ is symmetric under the symmetry group G. Coboundary transformations of this state are like local unitary (LU) operators that transform one state into another within the same SPT phase. Two cocycles that belong to a different cohomology sector, as classified by $\mathcal{H}^3(G, U(1))$, are not connected by a finite depth circuit of LUs. The case of $G = \mathbb{Z}_2$ has exactly two sectors $\mathcal{H}^3(G, U(1)) = \mathbb{Z}_2$.

3. Deformed Levin-Gu states

We choose the following 3-cochain:

$$\nu_3(g_i, g_j, g_k, 0) = CCZ(g_i, g_j, g_k)\frac{\lambda_2(g_j, g_k, 0)\lambda_2(g_i, g_j, 0)}{\lambda_2(g_i, g_k, 0)\lambda_2(g_i, g_j, g_k)},$$
$$\text{(E3)}$$

where $CCZ(g_i, g_j, g_k) = -1$ if $g_i = g_j = g_k = 1$ and $CCZ(g_i, g_j, g_k) = 1$ elsewhere. Here λ_2 is a 2-cochain parametrized by four independent phases $\lambda_2(g_i, g_j, 0)$ $(i, j = 0, 1)$.

The cocycle wave function (E2) has the form of Eq. (1) where U_A, U_B, and U_{AB} are diagonal in the basis $|\{g_i\}\rangle$, $U_{A,B,AB} = \sum_{\{g_i\}} U_{A,B,AB}(\{g_i\})|\{g_i\}\rangle\langle\{g_i\}|$ and given by

$$U_{AB}(\{g_i\}) = \frac{\prod_{i=1}^{2L-2} \nu_3^{(-1)^i}(g_i, g_{i+1}, g_{i+2}, 0)}{\nu_3(g_1, g_{2L-1}, g_{2L}, 0)}$$
$$\times \nu_3(g_1, g_2, g_{2L}, 0),$$

$$U_A(\{g_i\}) = \frac{\prod_{i \text{ even}=2}^{2L-2} \nu_3(g_i, g_{i+2}, g_A, 0)}{\nu_3(g_2, g_{2L}, g_A, 0)},$$

$$U_B(\{g_i\}) = \frac{\prod_{i \text{ odd}=1}^{2L-3} \nu_3^{-1}(g_i, g_{i+2}, g_B, 0)}{\nu_3^{-1}(g_1, g_{2L-1}, g_B, 0)}. \quad \text{(E4)}$$

4. Symmetry operator

The total symmetry operator

$$X = \sum_{\{g_i\}, g_A, g_B} |\{1 - g_i\}, 1 - g_A, 1 - g_B\rangle\langle\{g_i\}, g_A, g_B| \quad \text{(E5)}$$

separates into $X = X_A X_B$. The effective symmetry acting on ρ_{edge} is $U_A^\dagger X_A U_A$. Using Eqs. (E4) and (E1), we see that U_A factorizes into a product of CCZ gates familiar from the Levin-Gu model, and an additional factor U^{λ_2} associated with the coboundary transformation

$$U_A = \prod_{ijk} U_{CCZ}^{ijk} \times U^{\lambda_2}. \quad \text{(E6)}$$

The latter factor U^{λ_2} consists of a product over many 2-cochains λ_2 acting on various triangles. It can be divided into two factors as $U^{\lambda_2} = U^{\lambda_2'} U^{\lambda_2''}$:

(i) $U^{\lambda_2'}$: The 2-cocycles $\lambda(g_i, g_j, g_k)$ act only on triangles in A within the 2-sphere. Due to the cochain condition $\lambda(g_i, g_j, g_k) = \lambda(1 - g_i, 1 - g_j, 1 - g_k)$, we have $U^{\lambda_2'}{}^{\dagger} X_A U^{\lambda_2'} = X_A$.

(ii) $U^{\lambda_2''}$: The 2-cocycles $\lambda(g_i, g_j, 0)$ act on triangles on the surface defined by a membrane extending into the 3-ball from ∂A,

$$U^{\lambda_2''} = \sum_{\{g_i\}} \frac{\prod_{i \text{ even}=2}^{2L-2} \lambda_2(g_i, g_{i+2}, 0)}{\lambda_2(g_2, g_{2L}, 0)} |\{g_i\}\rangle\langle\{g_i\}|. \quad (E7)$$

Since the symmetry operator X does not act on the interior of the 3-ball, these are nontrivial.

As a result, we obtain

$$U^{\lambda_2''}{}^{\dagger} X U^{\lambda_2''}$$
$$= X \times \sum_{\{g_i\}} \frac{\prod_{i \text{ even}=2}^{2L-2} \frac{\lambda_2(g_i, g_{i+2}, 0)}{\lambda_2(1-g_i, 1-g_{i+2}, 0)}}{\frac{\lambda_2(g_2, g_{2L}, 0)}{\lambda_2(1-g_2, 1-g_{2L}, 0)}} |\{g_i\}\rangle\langle\{g_i\}|. \quad (E8)$$

As a result, the edge symmetry operator is

$$S_{\text{edge}} = \prod_{i \in \text{even}} X_i \prod_{i \in \text{even}} Z_i \prod_{i \in \text{even}} U_{CZ}^{i,i+2}$$
$$\times \sum_{\{g_i\}} \frac{\prod_{i \text{ even}=2}^{2L-2} \frac{\lambda_2(g_i, g_{i+2}, 0)}{\lambda_2(1-g_i, 1-g_{i+2}, 0)}}{\frac{\lambda_2(g_2, g_{2L}, 0)}{\lambda_2(1-g_2, 1-g_{2L}, 0)}} |\{g_i\}\rangle\langle\{g_i\}|. \quad (E9)$$

This formula is used to determine the parity eigenvalue in Figs. 6 and 7.

APPENDIX F: FLUX PARAMETERS FIT

To fit the parameters $\phi(\theta), \varphi(\theta)$ to the ES, we solve a system of linear equations. After scaling and shifting the ES, it matches Eq. (32). To find the scaling coefficients and $\phi(\theta), \varphi(\theta)$, we write linear equations for the scaled levels $a(\xi_i - \xi_0)$. To obtain a, ϕ, φ, we construct explicit equations for the levels $(l, m) = (\pm 1, 0), (0, \pm 1)$, which we denote r_i. By simple algebra, one gets linear equations for a, ϕ, φ by equating the scaled ES to the CFT spectrum such that $a(\xi_{r_1} - \xi_0) = 0.5(1 - \phi)^2 - 0.5\phi^2 = 0.5 - \phi$. Hence, we get four equations:

$$a = \frac{0.5 - \phi}{\xi_{r_1} - \xi_0} = \frac{0.5 + \phi}{\xi_{r_2} - \xi_0} = \frac{0.5 - \varphi}{\xi_{r_3} - \xi_0} = \frac{0.5 + \varphi}{\xi_{r_4} - \xi_0}. \quad (F1)$$

Assuming no degeneracies exist, there are enough linear equations. We now write it in a matrix form

$$\begin{pmatrix} 1 & \frac{1}{\xi_{r_1} - \xi_0} & 0 \\ 1 & \frac{-1}{\xi_{r_2} - \xi_0} & 0 \\ 1 & 0 & \frac{1}{\xi_{r_3} - \xi_0} \end{pmatrix} \begin{pmatrix} a \\ \phi \\ \varphi \end{pmatrix} = \begin{pmatrix} \frac{1}{2(\xi_{r_1} - \xi_0)} \\ \frac{1}{2(\xi_{r_2} - \xi_0)} \\ \frac{1}{2(\xi_{r_3} - \xi_0)} \end{pmatrix}. \quad (F2)$$

Solving these equations, we get a, ϕ, φ for each θ value. These equations require a guess for the indices r_1, r_2, r_3, and one has the freedom to choose three of the four available equations.

Let us focus on the results in Fig. 7. For θ near 0 in Fig. 7(a), we choose $r_1 = 1, r_3 = 2, r_4 = 3$ and solve their corresponding equations. Similarly, for θ near $\frac{\pi}{2}$ in Fig. 7(b), we choose $r_1 = 2, r_2 = 4, r_3 = 1$. In both cases the results show a linear behavior for $\phi(\theta)$ and quadratic behavior for $\varphi(\theta)$.

ϕ, φ have symmetries due to the CFT spectrum. Specifically, $\phi \to -\phi$ and $\varphi \to -\varphi$ do not change the ES as changing m, l accordingly $m \to -m, l \to -l$ preserves the ES. Similarly, $\phi \to \phi + 1, \varphi \to \varphi + 1$ still keeps the ES the same as $m \to m - 1, l \to l - 1$, respectively. These symmetries allow us to choose $0 \leqslant \phi, \varphi < 1$.

[1] X. Chen and X.-G. Wen, Chiral symmetry on the edge of 2D symmetry protected topological phases, Phys. Rev. B **86**, 235135 (2012).

[2] M. Levin and Z.-C. Gu, Braiding statistics approach to symmetry-protected topological phases, Phys. Rev. B **86**, 115109 (2012).

[3] L. H. Santos and J. Wang, Symmetry-protected many-body Aharonov-Bohm effect, Phys. Rev. B **89**, 195122 (2014).

[4] T. Scaffidi and Z. Ringel, Wave functions of symmetry-protected topological phases from conformal field theories, Phys. Rev. B **93**, 115105 (2016).

[5] B. Han, A. Tiwari, C.-T. Hsieh, and S. Ryu, Boundary conformal field theory and symmetry-protected topological phases in 2 + 1 dimensions, Phys. Rev. B **96**, 125105 (2017).

[6] M. Goldstein and E. Sela, Symmetry-Resolved Entanglement in Many-Body Systems, Phys. Rev. Lett. **120**, 200602 (2018).

[7] J. C. Xavier, F. C. Alcaraz, and G. Sierra, Equipartition of the entanglement entropy, Phys. Rev. B **98**, 041106(R) (2018).

[8] R. Bonsignori, P. Ruggiero, and P. Calabrese, Symmetry resolved entanglement in free fermionic systems, J. Phys. A: Math. Theor. **52**, 475302 (2019).

[9] P. Calabrese, J. Dubail, and S. Murciano, Symmetry-resolved entanglement entropy in wess-zumino-witten models, J. High Energy Phys. 10 (2021) 067.

[10] R. Islam, R. Ma, P. M. Preiss, M. E. Tai, A. Lukin, M. Rispoli, and M. Greiner, Measuring entanglement entropy in a quantum many-body system, Nature (London) **528**, 77 (2015).

[11] A. Neven, J. Carrasco, V. Vitale, C. Kokail, A. Elben, M. Dalmonte, P. Calabrese, P. Zoller, B. Vermersch, R. Kueng *et al.*, Symmetry-resolved entanglement detection using partial transpose moments, npj Quantum Inf. **7**, 152 (2021).

[12] V. Vitale, A. Elben, R. Kueng, A. Neven, J. Carrasco, B. Kraus, P. Zoller, P. Calabrese, B. Vermersch, and M. Dalmonte, Symmetry-resolved dynamical purification in synthetic quantum matter, SciPost Phys. **12**, 106 (2022).

[13] A. Rath, V. Vitale, S. Murciano, M. Votto, J. Dubail, R. Kueng, C. Branciard, P. Calabrese, and B. Vermersch, Entanglement

barrier and its symmetry resolution: Theory and experiment observation, PRX Quantum **4**, 010318 (2023).

[14] D. Azses, R. Haenel, Y. Naveh, R. Raussendorf, E. Sela, and E. G. Dalla Torre, Identification of Symmetry-Protected Topological States on Noisy Quantum Computers, Phys. Rev. Lett. **125**, 120502 (2020).

[15] D. Azses, E. G. Dalla Torre, and E. Sela, Observing floquet topological order by symmetry resolution, Phys. Rev. B **104**, L220301 (2021).

[16] D. Azses and E. Sela, Symmetry-resolved entanglement in symmetry-protected topological phases, Phys. Rev. B **102**, 235157 (2020).

[17] F. Pollmann, A. M. Turner, E. Berg, and M. Oshikawa, Entanglement spectrum of a topological phase in one dimension, Phys. Rev. B **81**, 064439 (2010).

[18] E. Cornfeld, L. A. Landau, K. Shtengel, and E. Sela, Entanglement spectroscopy of non-abelian anyons: Reading off quantum dimensions of individual anyons, Phys. Rev. B **99**, 115429 (2019).

[19] D. V. Else, I. Schwarz, S. D. Bartlett, and A. C. Doherty, Symmetry-Protected Phases for Measurement-Based Quantum Computation, Phys. Rev. Lett. **108**, 240505 (2012).

[20] R. Raussendorf and H. J. Briegel, A One-Way Quantum Computer, Phys. Rev. Lett. **86**, 5188 (2001).

[21] H. Li and F. D. M. Haldane, Entanglement Spectrum as a Generalization of Entanglement Entropy: Identification of Topological Order in Non-Abelian Fractional Quantum Hall Effect States, Phys. Rev. Lett. **101**, 010504 (2008).

[22] X.-L. Qi, H. Katsura, and A. W. W. Ludwig, General Relationship between the Entanglement Spectrum and the Edge State Spectrum of Topological Quantum States, Phys. Rev. Lett. **108**, 196402 (2012).

[23] L. Zou and J. Haah, Spurious long-range entanglement and replica correlation length, Phys. Rev. B **94**, 075151 (2016).

[24] M. J. Arildsen, N. Schuch, and A. W. Ludwig, Entanglement spectra of non-chiral topological $(2 + 1)$-dimensional phases with strong time-reversal breaking, Li-Haldane state counting, and PEPS, arXiv:2207.03246.

[25] F. Verstraete, V. Murg, and J. Cirac, Matrix product states, projected entangled pair states, and variational renormalization group methods for quantum spin systems, Adv. Phys. **57**, 143 (2008).

[26] J. Eisert, Entanglement and tensor network states, Model. Simul. **3**, 520 (2013).

[27] R. Orús, A practical introduction to tensor networks: Matrix product states and projected entangled pair states, Ann. Phys. **349**, 117 (2014).

[28] N. Feldman, A. Kshetrimayum, J. Eisert, and M. Goldstein, Entanglement estimation in tensor network states via sampling, PRX Quantum **3**, 030312 (2022).

[29] X. Chen, Z.-C. Gu, Z.-X. Liu, and X.-G. Wen, Symmetry protected topological orders and the group cohomology of their symmetry group, Phys. Rev. B **87**, 155114 (2013).

[30] P. Calabrese and J. Cardy, Entanglement entropy and quantum field theory, J. Stat. Mech. (2004) P06002.

[31] X. Chen, Z.-C. Gu, and X.-G. Wen, Classification of gapped symmetric phases in one-dimensional spin systems, Phys. Rev. B **83**, 035107 (2011).

[32] Z.-W. Liu and A. Winter, Many-body quantum magic, PRX Quantum **3**, 020333 (2022).

[33] M. Fishman, S. R. White, and E. M. Stoudenmire, The ITensor software library for tensor network calculations, SciPost Phys. Codebases **4** (2022).

[34] J. C. Y. Teo and C. L. Kane, From luttinger liquid to non-abelian quantum hall states, Phys. Rev. B **89**, 085101 (2014).

[35] A. J. A. James and R. M. Konik, Understanding the entanglement entropy and spectra of 2D quantum systems through arrays of coupled 1D chains, Phys. Rev. B **87**, 241103(R) (2013).

[36] J. Cano, T. L. Hughes, and M. Mulligan, Interactions along an entanglement cut in $2 + 1$D abelian topological phases, Phys. Rev. B **92**, 075104 (2015).

[37] T. Neupert, C. Chamon, C. Mudry, and R. Thomale, Wire deconstructionism of two-dimensional topological phases, Phys. Rev. B **90**, 205101 (2014).

[38] Y.-M. Lu and A. Vishwanath, Theory and classification of interacting integer topological phases in two dimensions: A chern-simons approach, Phys. Rev. B **86**, 125119 (2012).

[39] T. Meng, T. Neupert, M. Greiter, and R. Thomale, Coupled-wire construction of chiral spin liquids, Phys. Rev. B **91**, 241106(R) (2015).

[40] G. Gorohovsky, R. G. Pereira, and E. Sela, Chiral spin liquids in arrays of spin chains, Phys. Rev. B **91**, 245139 (2015).

[41] E. Leviatan and D. F. Mross, Unification of parton and coupled-wire approaches to quantum magnetism in two dimensions, Phys. Rev. Res. **2**, 043437 (2020).

[42] D. Poilblanc, Entanglement Spectra of Quantum Heisenberg Ladders, Phys. Rev. Lett. **105**, 077202 (2010).

[43] I. Peschel and M.-C. Chung, On the relation between entanglement and subsystem hamiltonians, Europhys. Lett. **96**, 50006 (2011).

[44] A. M. Läuchli and J. Schliemann, Entanglement spectra of coupled $s = \frac{1}{2}$ spin chains in a ladder geometry, Phys. Rev. B **85**, 054403 (2012).

[45] M. Mancini, G. Pagano, G. Cappellini, L. Livi, M. Rider, J. Catani, C. Sias, P. Zoller, M. Inguscio, M. Dalmonte, and L. Fallani, Observation of chiral edge states with neutral fermions in synthetic hall ribbons, Science **349**, 1510 (2015).

[46] A. Petrescu and K. Le Hur, Chiral mott insulators, meissner effect, and laughlin states in quantum ladders, Phys. Rev. B **91**, 054520 (2015).

[47] E. Cornfeld and E. Sela, Chiral currents in one-dimensional fractional quantum hall states, Phys. Rev. B **92**, 115446 (2015).

[48] M. Calvanese Strinati, E. Cornfeld, D. Rossini, S. Barbarino, M. Dalmonte, R. Fazio, E. Sela, and L. Mazza, Laughlin-like States in Bosonic and Fermionic Atomic Synthetic Ladders, Phys. Rev. X **7**, 021033 (2017).

[49] M. Calvanese Strinati, S. Sahoo, K. Shtengel, and E. Sela, Pretopological fractional excitations in the two-leg flux ladder, Phys. Rev. B **99**, 245101 (2019).

[50] J. C. Bridgeman and C. T. Chubb, Hand-waving and interpretive dance: an introductory course on tensor networks, J. Phys. A: Math. Theor. **50**, 223001 (2017).

[51] M. Hastings, Notes on some questions in mathematical physics and quantum information, arXiv:1404.4327.